Supporting Information

Exploring a Scalable Route for Efficient Flexible Perovskite Solar Cells via Amphiphilic Cross-linkable Monomer

Chenfan Xing[1,2†], Weifu Zhang[3†], Hengyu Zhou[2†], Jiahan Xie[2], Shuaizhen Huang[2], Simeng Gao[2], Leixi He[2], Zhongqiang Wang[1,4], Lin Xie[5*], Mengjin Yang[2], Wei Song[2*], Ziyi Ge[2*]*

[1] College of Physics and Optoelectronics, Ministry of Education Key Laboratory of Interface Science and Engineering in Advanced Materials, Taiyuan University of Technology, Taiyuan 030024, China

[2] Zhejiang Provincial Engineering Research Center of Energy Optoelectronic Materials and Devices, Ningbo Institute of Materials Technology & Engineering, Chinese Academy of Sciences, Ningbo 315201, China.

[3] CAS Key Laboratory of Green Printing, Institute of Chemistry, Chinese Academy of Sciences Beijing 100190, China.

[4] School of Integrated Circuits, Ludong University, Yantai, 264025, China.

[5] School of Physical Science and Technology and School of Resources, Environments and Materials, Guangxi University, Nanning, Guangxi530004, China.

* Corresponding authors.

E-mail:wangzhongqiang@tyut.edu.cn;20250153@gxu.edu.cn;songwei@nimte.ac.cn; geziyi@nimte.ac.cn

† These authors contributed equally to this work.

Experimental Sections

1. Materials

Solvents: N, N-dimethyl formamide (DMF, anhydrous, ≥99.8%), Dimethyl sulfoxide (DMSO, anhydrous, ≥99.9%) were purchased from Sigma-Aldrich (USA). Diethyl ether (DE, anhydrous, 99.7%), Absolute ethanol (General-Reagent, 99.7%), Acetone (99.5%) and isopropanol (IPA, 99.7%) were purchased from Sinopharm Chemical Reagent Co., Ltd (China).

Reagents: (4-(7H-dibenzo[c,g]carbazol-7-yl)butyl)phosphonic acid (4PADCB, ≥99.8%) , Fullerene C60 (C60, ≥99.5%), Bathocuproine (BCP, ≥99.5%) were purchased from Shanghai Daeyeon Chemical Corp (China). Patterned Glass/ITO substrate, Cesium iodide (CsI, 99.99%), Formamidinium iodide (FAI, 99.9%), Methylammonium bromide (MABr, 99.99%), Lead(II) iodide (PbI_2, 99.99%), Lead bromide ($PbBr_2$, 99.99%) and methylammonium chloride (MACl, 99.9%) were purchased from Advanced Election Technology Corp (China). The key feedstock 5-(1,2-dithiolan-3-yl)pentanamide(TAN)and1-{2-[(E)-[4-(dihydroxyboranyl)phenyl]methylidene]diazanyl}-5-(1,2-dithiolan-3-yl)pentan-1-one(TBA) were purchased from Zhengzhou Alfa Chemical Co., Ltd. with a purity of 97%.
All the chemicals and reagents were purchased and used directly without any further purification

2. Solution Preparation

The 1.62 M perovskite precursor solution with the composition of $Cs_{0.05}(FA_{0.98}MA_{0.02})_{0.95}(I_{0.95}Br_{0.05})_3$ was prepared by fully dissolving FAI, MABr, CsI, PbI_2, $PbBr_2$ in a mixed solvent of DMF and DMSO with a volume ratio of 4:1. Moreover, for the precursor solution with CL(TAN) and CL(TBA), 0.3 mg of TAN and TBA was introduced into the perovskite precursor solution, respectively. Then, the perovskite precursor solution was stirred at room temperature for 6 hours..

3. Device fabrication

Firstly, the patterned glass/indium tin oxide (ITO) substrates were washed with detergent, deionized water, acetone, and isopropanol in sequence for 20 minutes. After that, the cleaned substrates were dried by nitrogen (N_2) flow and then treated with oxygen plasma for 5 minutes. The prepared devices with a architecture of Glass /ITO/4PADCB/PVK/C60/ BCP/Ag. In terms of the preparation of rigid device, 100 ul 4PADCB (0.8mg/ml) dissolved in absolute ethanol was spin coated on ITO for 30 s at 3000 rpm, and then annealed at 120 ℃ for 10 minutes.

Subsequently, 50 ul perovskite precursor solution was deposited on 4PADCB-based substrate at 4000 rpm for 30 s, 600 ul DE as the antisolvent was added dropwise onto the center of substrate at 15 s before the end of spin-coating. The as-prepared perovskite films were immediately transferred to hotplate and annealed at 100 ℃ for 30 min. For the devices with post- treatment, 100 μl of PI (1.0 mg/ml) dissolved in IPA was spin-coated on the perovskite surface at 5000 rpm for 25 s, followed by annealing at 100 °C for 5 minutes. The aforementioned spin-coated processes were all conducted at room temperature (25-30 ℃) in a N_2-filled glove box with the contents of O_2 and H_2O < 0.01 ppm. Finally, 25 nm of C60 at a rate of 0.2 Å/s, 10 nm of BCP at a rate of 0.2 Å/s, and 100 nm of silver (Ag) electrode at a rate of 2.0 Å/s were thermally evaporated, respectively, under high vacuum ($<1 \times 10^{-4}$ pa).

4. Modules-fabrication process

For the fabrication of perovskite solar modules (PSMs), the primary difference compared to small-area device fabrication is that the modules involve additional scribing steps to divide a large-area device into small-area subcells and form electrical interconnections between them. The scribing scheme includes three basic steps (known as P1, P2 and P3 scribing). The P1 pattern is etched on glass/ITO substrates by laser, a femtosecond infrared laser (1030nm, 400fs, 0.5MHz, scribing speed 2000mm/s, average power 10.063W), and then the substrates are cleaned using the aforementioned methods. The 4PADCB/PVK/C60/BCP layers are subsequently deposited on the substrates. In terms of the preparation of rigid device, 300 ul 4PADCB (0.8mg/ml) dissolved in absolute ethanol was spin coated on ITO for 30 s at 4000 rpm, and then annealed at 120 ℃ for 10 minutes. Subsequently, 150 ul perovskite precursor solution was deposited on 4PADCB-based substrate at 5000 rpm for 30 s, 3000 ul DE as the antisolvent was added dropwise onto the center of substrate at 15 s before the end of spin-coating. The as-prepared perovskite films were immediately transferred to hotplate and annealed at 100 ℃ for 30 min. For the devices with post-treatment, 300 μl of PI (1.0 mg/ml) dissolved in IPA was spin-coated on the perovskite surface at 6000 rpm for 25 s, followed by annealing at 100 °C for 5 minutes. The P2 scribing step removes the BCP/C60/PVK/4PADCB layers, exposing the ITO within the P2 pattern lines (1030nm, 400fs, 0.5MHz, scribing speed 2000mm/s, average power 3.123W). Afterward, 100 nm of Ag was deposited by thermal evaporation, covering the top of ETL and filling the P2 channels. Finally, the P3 scribing step is conducted to isolate the Ag electrode between neighbouring subcells, using the same laser with 4.858W average power and scribing speed 3000mm/s, completing the monolithic interconnections.

5. Characterizations of films

The Fourier transform infrared (FTIR) spectroscopy was detected by FTIR8400S (Shimadzu). The X-ray photoelectron spectroscopy (XPS) experiments were recorded on a monochromatic Al-Kα (1486.6 eV) as the radiation source (Shimadzu, Axis Supra). The Scanning Electron Microscope (SEM) (verios G4 UC) (Rimono Scientific Company, America) was performed at 2kV to obtain the top-view and cross-sectional SEM images of perovskite films. X-Ray diffraction (XRD) measurements were performed using a D/MAX Ultima III XRD spectrometer (Rigaku) with a Cu Kα line of λ = 1.5410 Å. Grazing incident wide-angle X-ray scattering (GIWAXS) measurements were performed by the XEUSS SAXS/WAXS equipment, at an incident angle of 0.5º. The Atomic Force Microscopy (AFM) images, Kelvin Probe Force Microscopy (KPFM) images and the peak force quantitative nanomechanical atomic force microscopy (PFQNM-AFM) were captured by Bruker Dimension ICON SPM, America. The energy level was obtained by ultra-violet photoelectron spectroscopy (UPS) (R3000, Scienta) using HeI (21.2 eV) as the excitation source and ultraviolet-visible absorption spectra (UV-vis) (Lambda 950). The steady photoluminescence (PL) spectra were obtained from the Horiba jobin Yvon fluorolog-3 spectrofluorometer system with incident light at 405nm and the time-resolved photoluminescence (TRPL) was analyzed by the FLS 980 fluorescence spectrometer equipped with a 475 nm excitation. PL mapping was measured by LEICA TCS SP5.

6. Characterizations of devices

The photovoltaic performance of the device was measured under simulated solar lamp (100 mW/cm^2, AM1.5 G) provided by Newport oriel sol3A 450 W solar simulator. The J-V curves of devices were measured at room temperature The light source parameters are 450 W xenon lamp (oriel solar simulator), calibrated to 100 mW/cm^2 by silicon reference cell. The effective area is 0.06 cm^2, defined with a non-reflective mask. The scanning parameters were forward scanning (-0.2 to 1.2 V, step 0.02 V, scan rate : 0.1 V/s dwell time 50 ms) and reverse scanning (from 1.2 to -0.2 V, step 0.02 V, scan rate : 0.1 V/s dwell time 50 ms). The stabilized power output (SPO) and steady-state current density curves of the devices were measured by detecting the photocurrent density output with the biased voltage set at the MPP. The dependence of V_{oc}/J_{sc} on light intensity were measured by varying the light intensity. The solar cell quantum efficiency test system (Elli Technology Taiwan) was used to measure the EQE spectra of devices with a wavelength range of 300~1100 nm. The capacitance versus frequency (C–F) curves were recorded by the 1240A Impedance Analyzer. The Mott-Schottky curves and the impedance spectroscopy (IS) were determined with the Chenhua CHI760E electrochemical

workstation. EQE_{EL} measurements were measured by applying external voltage/current sources through the PSCs with a REPS measurement instrument (Enlitech). The operational stability of the devices was also examined by monitoring the maximum power point (MPP) tracking under 1 sun illumination in an N_2 environment (~25 ℃ and ~30% RH).

7. Theoretical simulation

The Density Functional Theory (DFT) calculations in this work are performed using the Vienna ab initio simulation software (VASP). The exchange-functional was treated using the Perdew-Burke-Ernzerhof (PBE) functional, in combination with the DFT-D3 correction. Cut-off energy of the plane-wave basis was set as 450 eV. For optimization of lattice size of $FAPbI_3$ cubic cell, the Brillouin Zone integration was performed with a Monkhorst-Pack k-point sampling of 4×4×4. For optimization of geometry of slab models, the Brillouin Zone integration was performed with a Gamma k-point sampling of 1×1×1. The self-consistent calculations applied a convergence energy threshold of 10^{-5} eV. After completing the structural optimization calculation, the adsorption energies (E_{ads}) and formation energies (E_f) of defects were calculated by the equation as follows:

$E_{ads} = E(AB) - E(A) - E(B)$.

Where, *E(AB)* represents the total energy of slab model with TBA or TAN adsorbed on surface. E(*A*) represents the total energy of clean surface of slab model. E(B) represents the total energy of TAN or TBA molecule in its gas phase.

$E_f = E(C) + E(S)/n - E(D)$.

Here, *E(C)* represents the total energy of slab model with vacancy on surface. *E(D)* represents the total energy of slab model with no vacancy on surface. *E(S)* represents the total energy of stable element. n represents the total number of atoms of stable element. In the case of E_f of I vacancy, $E(S) = 0.5*E(I_2)$. In the case of E_f of Pb vacancy, $E(S) = 0.25*E(Pb_4)$. In the case of E_f of FA vacancy, $E(S) = 0.25*E(graphite(C_4)) + 2.5*E(H_2) + E(N_2)$. I_2, Pb_4, graphite(C_4), H_2 and N_2 are stable elements.

8. Calculation Methods

Note 1: Carrier recombination lifetime and exciton lifetime calculation

The carrier recombination lifetimes can be derived from time-resolved photoluminescence (TRPL), the TRPL decay curves were fitted by the bi-exponential function:

$$y(t) = A_1 exp^{\frac{-t}{\tau_1}} + A_2 exp^{\frac{-t}{\tau_2}} + y_0$$

$$\tau_{ave} = \frac{\sum A_i \tau_i^2}{\sum A_i \tau_i}$$

where, A_1 and A_2 are the relative amplitudes, τ_1 and τ_2 represent time constants for fast and slow decay lifetimes in relation to nonradiative recombination of surface traps near the GBs and radiative recombination from the bulk perovskite film, respectively.

Note 2: Analyzation of space-charge-limited current (SCLC) model

The dark *J-V* curves display three typical regions: (I) the Ohmic region at low bias region, (II) the trap-filled limited region at intermediate bias region, and (III) a trap-free SCLC region at high bias region. In the trap-filled limited region, the trap density levels are continuously filled as bias increases, and all of traps are filled until the trap-filled limit voltage (V_{TFL}). The trap density is estimated according to the equation:

$$N_t = \frac{2\varepsilon\varepsilon_0 V_{TFL}}{qL^2}$$

Where N_t is the trap density, ε is the dielectric constants of perovskite, ε_0 is the vacuum permittivity, L is the thickness of the perovskite film, and q the elementary charge. V_{TFL} is obtained by fitting the dark *I-V* data with the equation.

Note 3: The dependence of J_{sc} and V_{oc} of the PSCs on light intensity

The ideality factor nKT/q can be calculated by equation:

$$V_{oc} = \frac{nKT}{q} ln(P_{light})$$

The exponential factor α can be calculated by equation:

$$\alpha = \frac{ln(J_{sc})}{ln(P_{light})}$$

Note 4: Hysteresis index (HI)

The *J-V* hysteresis index (HI) is defined by the following equation:

$$HI = \frac{PCE_{Reverse} - PCE_{Forward}}{PCE_{Reverse}}$$

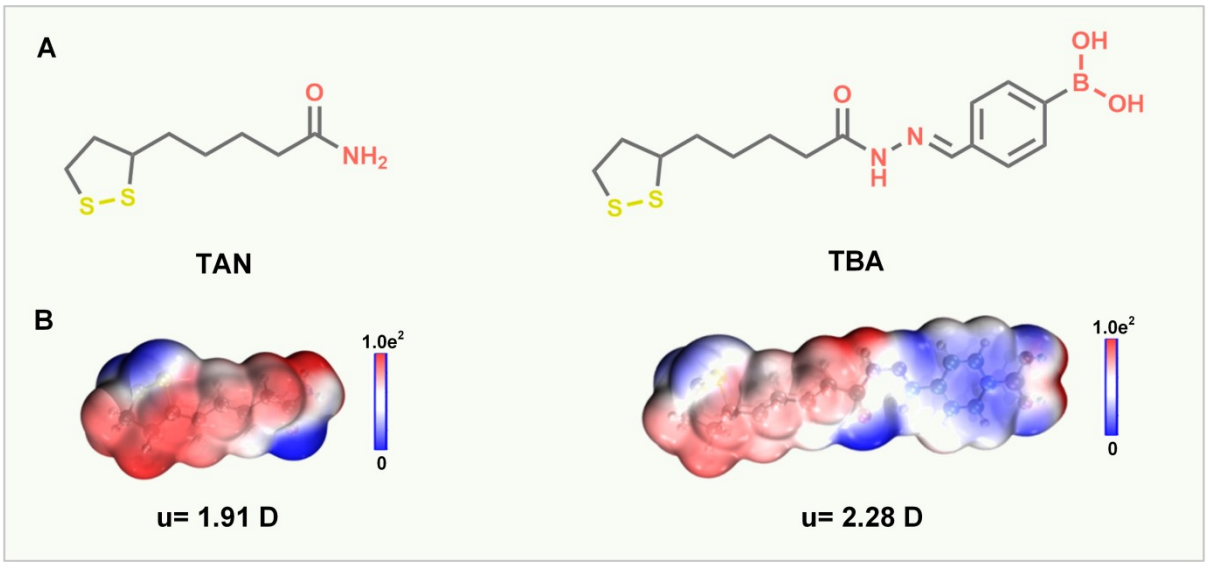

Figure S1. Molecule syructure (A) and calculated electrostatic potential (ESP) distributions (B) of TAN and TBA .

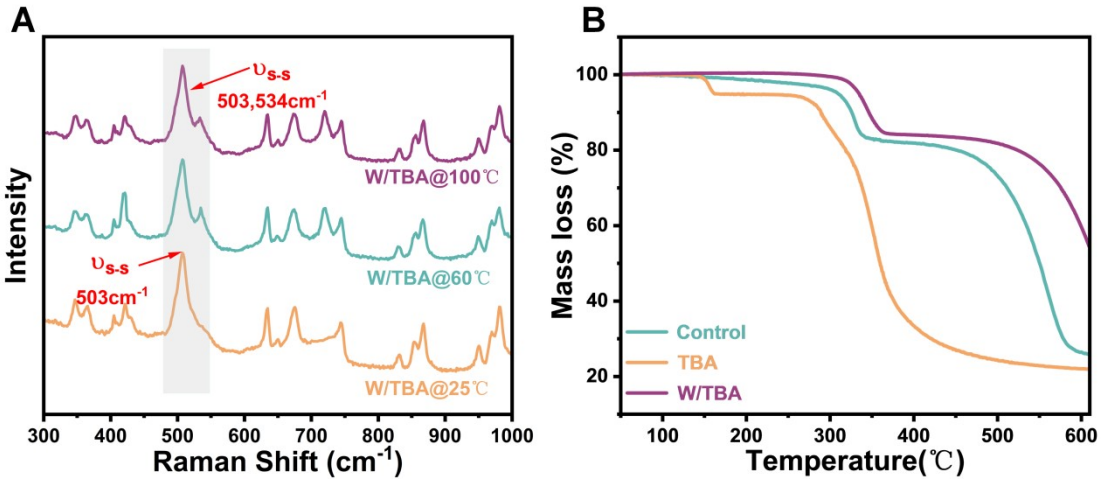

Figure S2. **Ring-opening polymerization process and thermal stability of TBA**. (A) Raman spectra of TBA heating at different temperatures. (B) TGA curves of the perovskite powder, TBA, and the perovskite powder containing TBA.

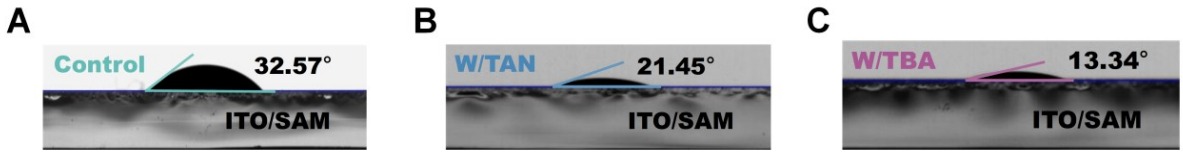

Figure S3. Contact angles of the perovskite precursor on the glass/ITO/SAM substrates.

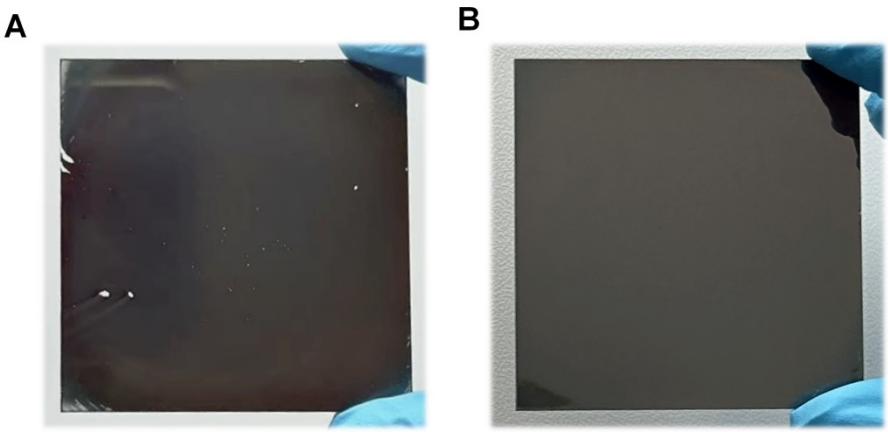

Figure S4. Photographic images of large-area perovskite films deposited on 5×5 cm^2 glass/ITO/SAMs substrates.

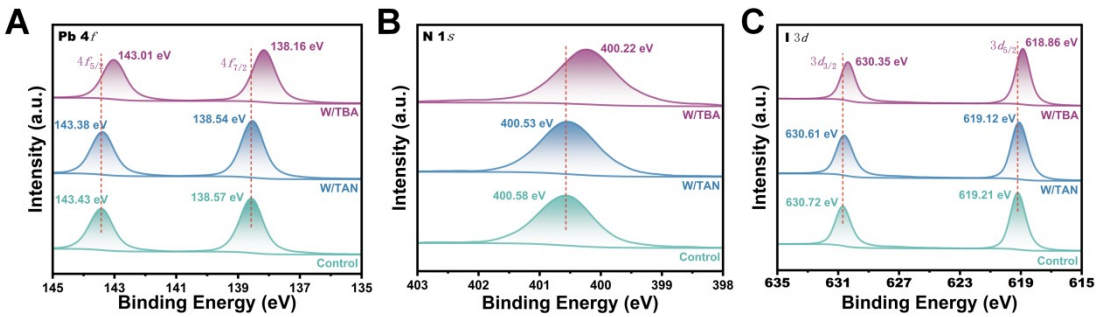

Figure S5. High-resolution XPS spectra of Pb 4*f*, N 1*s*, I 3*d* core levels for control, TAN- and TBA-modified perovskite films.

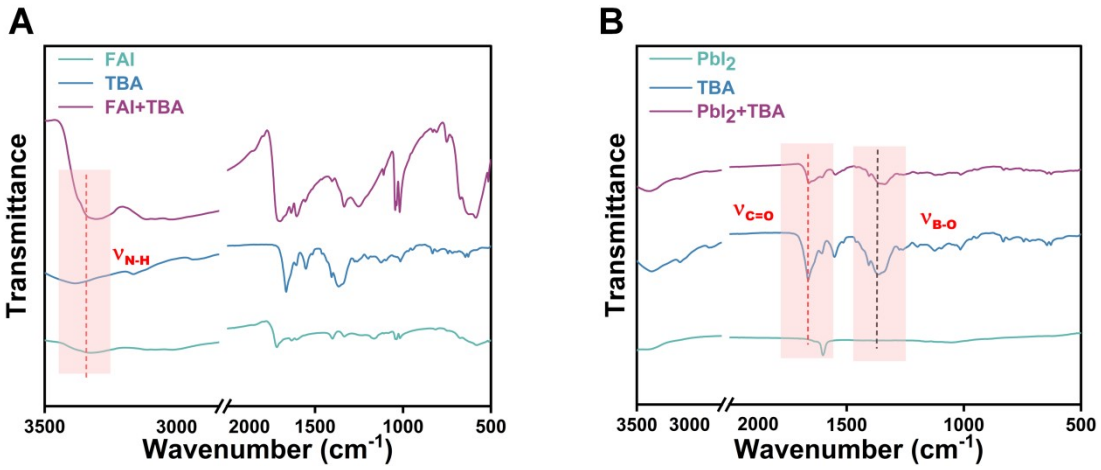

Figure S6. (A) FTIR spectra of pure PbI_2, TBA molecules, TBA and PbI_2 mixed powder. (B) FTIR spectra of pure FAI, TBA molecules, FAI and TBA mixed powder.

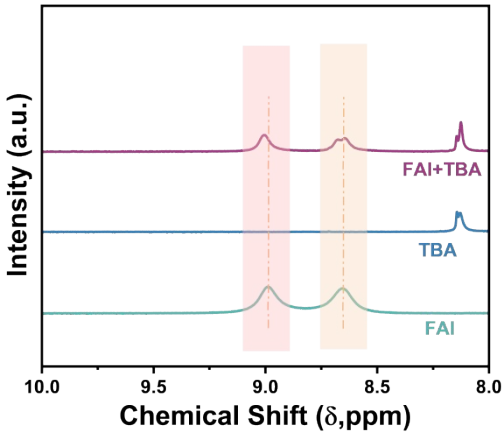

Figure S7. A comparison of 1H NMR spectra of FAI, TBA, TBA+FAI in deuterated d_6-DMSO.

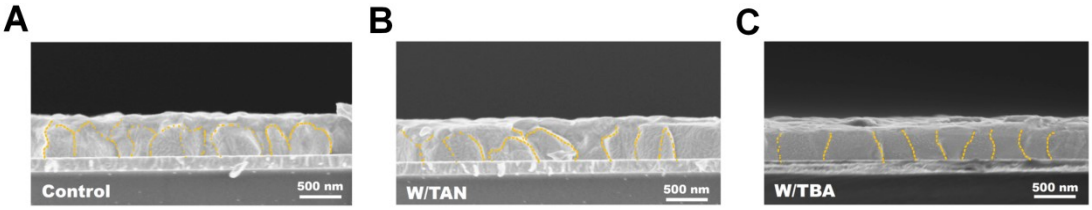

Figure S8. Cross-sectional SEM images of the perovskite films. (A) Control, (B) W/TAN modified perovskite film and (C)W/TBA-modified perovskite film.

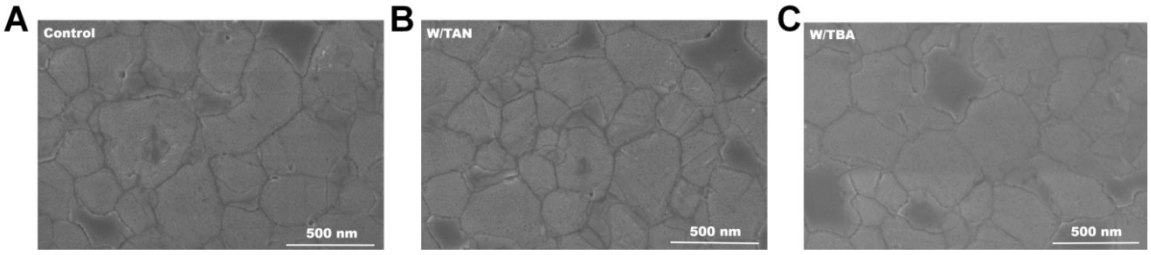

Figure S9. SEM images of buried interface. (A) Control, (B) W/TAN, and (C) W/TBA.

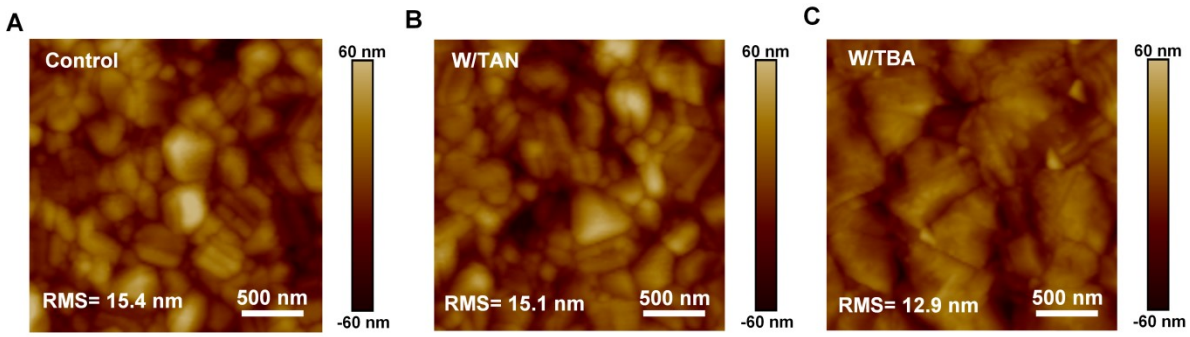

Figure S10. AFM images of (A) control, (B) TAN-modified, and (C) TBA-modified perovskite films.

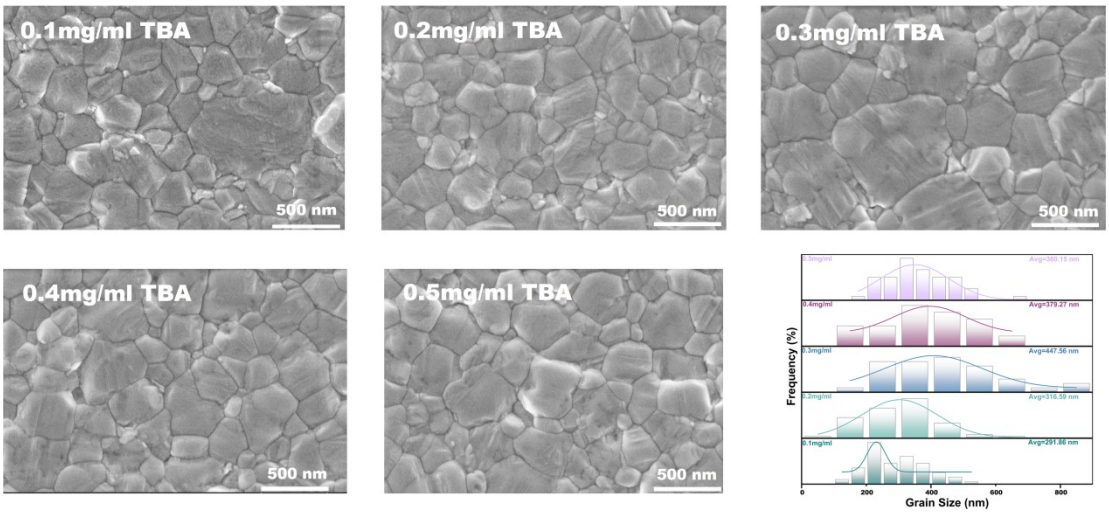

Figure S11. SEM images of perovskite films with different concentrations of TBA

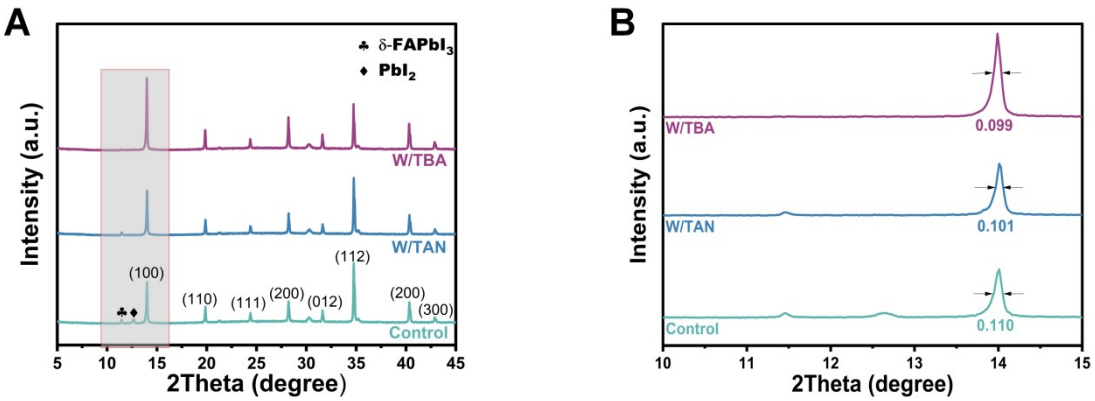

Figure S12. **XRD patterns of perovskite films.** (A) XRD patterns of Control, TAN- and TBA-modified perovskite films. (B) XRD patterns of the range of 10-15° and the corresponding FWHM of the perovskite films.

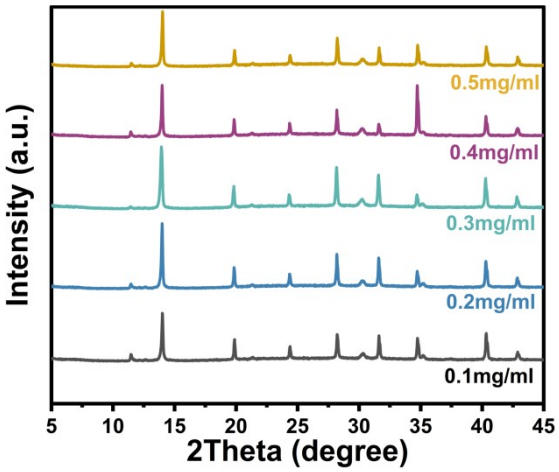

Figure S13. XRD patterns of perovskite film with different concentrations of TBA. The highest intensity of diffraction peak was observed for the perovskite films with 0.3 mg mL^{-1} TBA, this result is consistent with the trend shown in SEM images, indicates that 0.3 mg mL^{-1} is the most optimal addition amount.

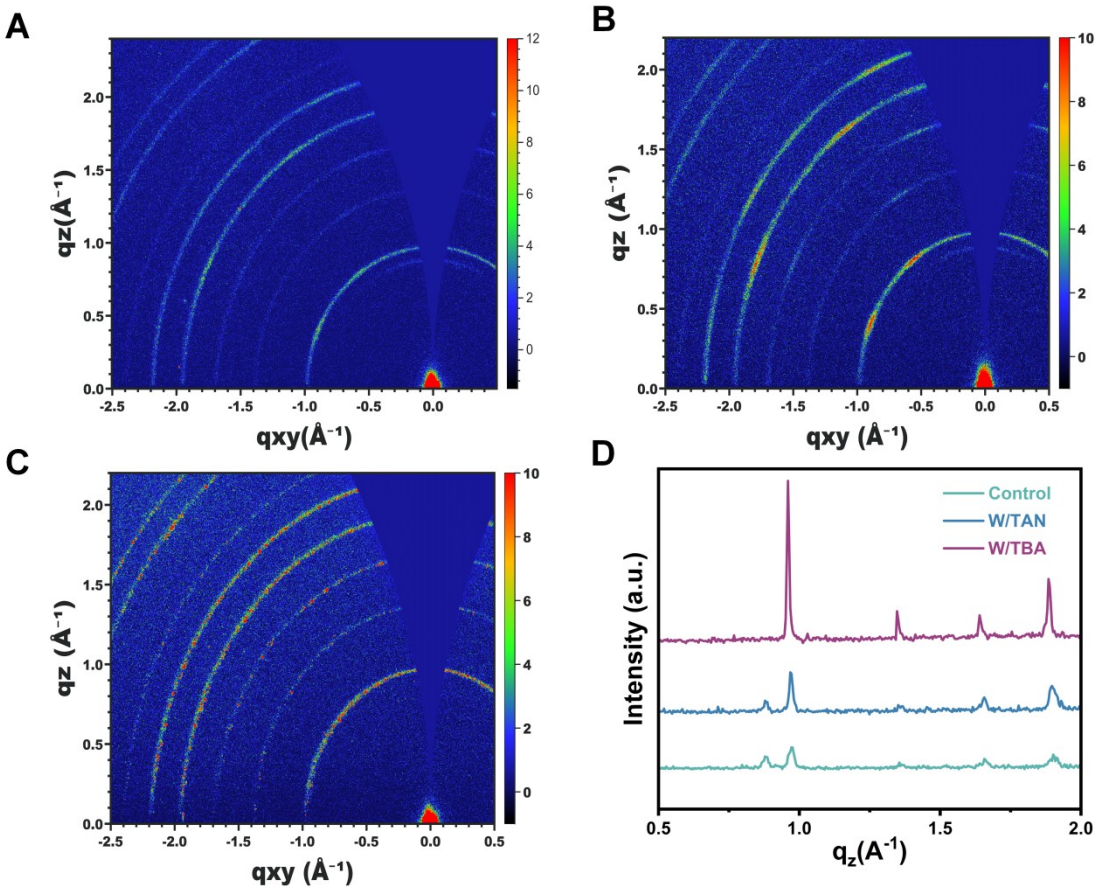

Figure S14. 2D-GIWAXS patterns of Control (A) TAN- (B) and TBA-treated (C) perovskite films. (D) The corresponding out-of-plane line cuts of GIWAXS patterns.

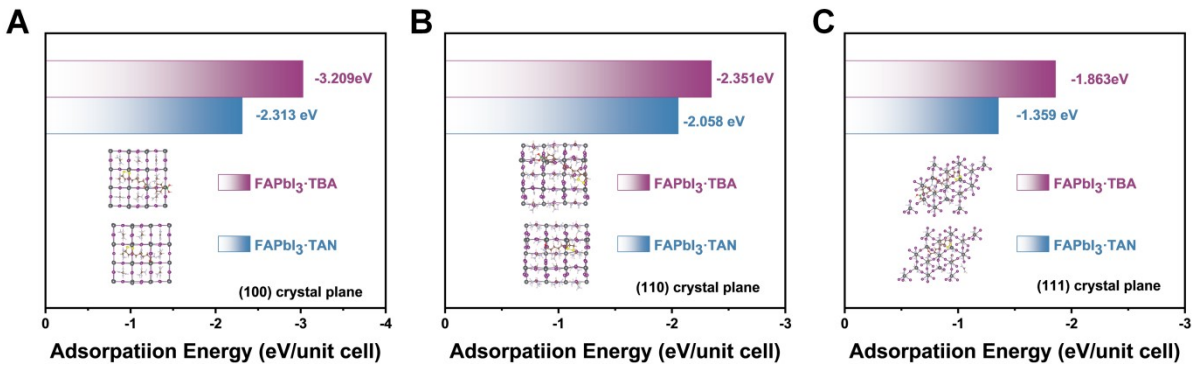

Figure S15. **Adsorption models and corresponding adsorption energies of TAN and TBA on different crystal planes of perovskite**. (A) (100) crystal plane. (B) (110) crystal plane. (C) (111) crystal plane.

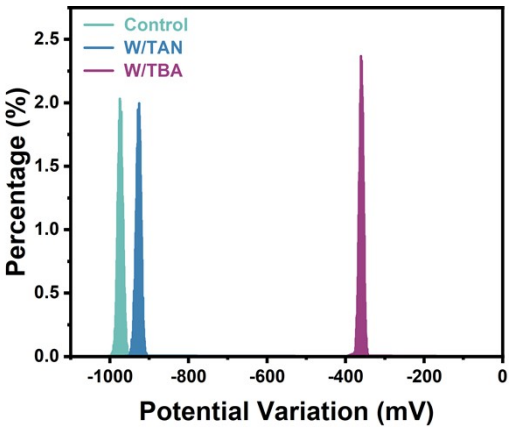

Figure S16. Surface potential variation of perovskite films.

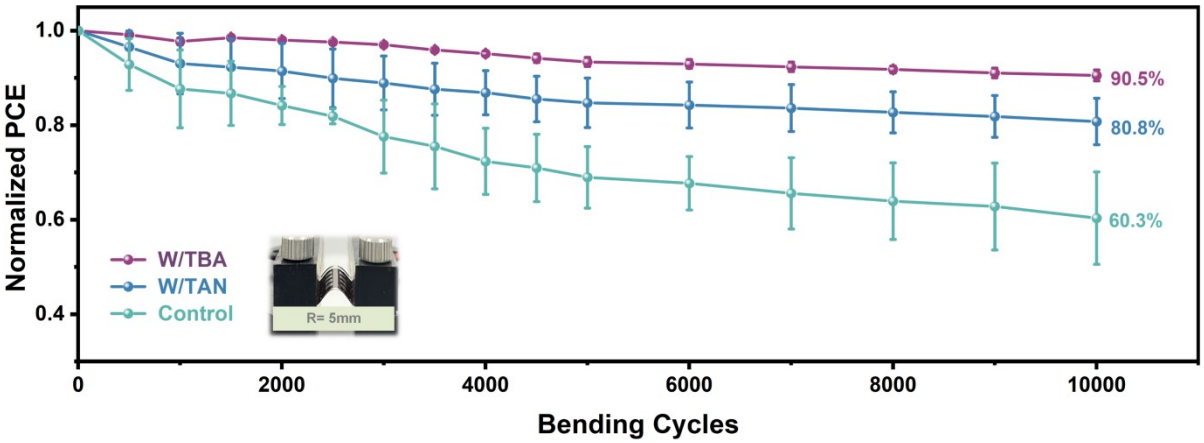

Figure S17. Mechanical stability of the f-PSCs versus bending cycles at a radius of 5 mm.

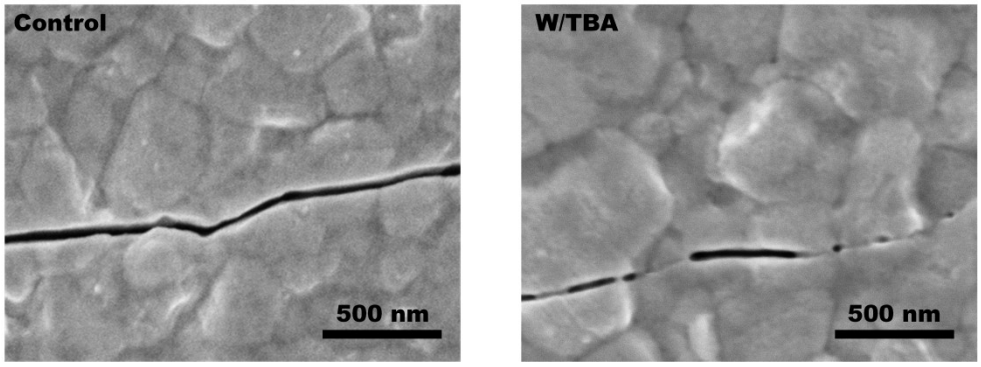

Figure S18. Top-view SEM images of the perovkite films after 10000 bending cycles.

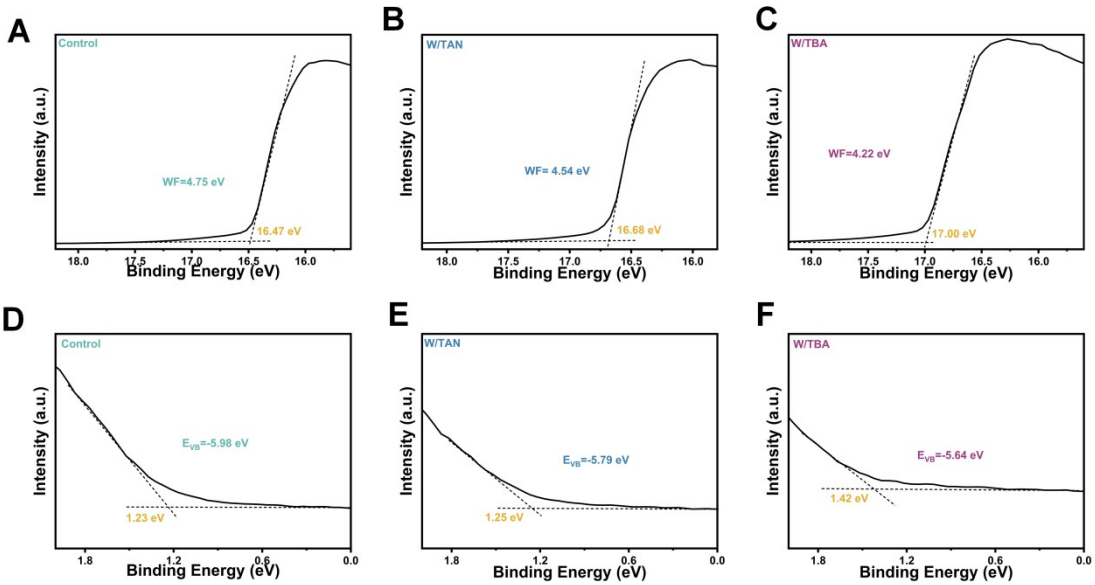

Figure S19. UPS spectra of perovskite films. (A-C) in the secondary-cutoff region. (D-F) in the valance band region.

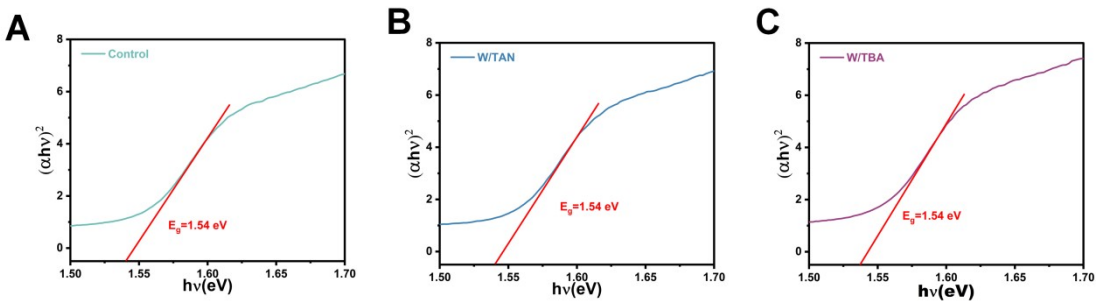

Figure S20. The UV-vis absorbance spectrum of the (A) Control, (B) TAN- and (C) TBA-treated perovskite films.

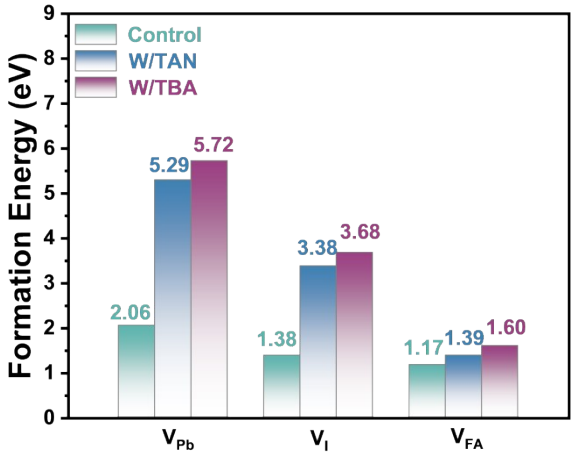

Figure S21. Calculated formation energy of different types defects.

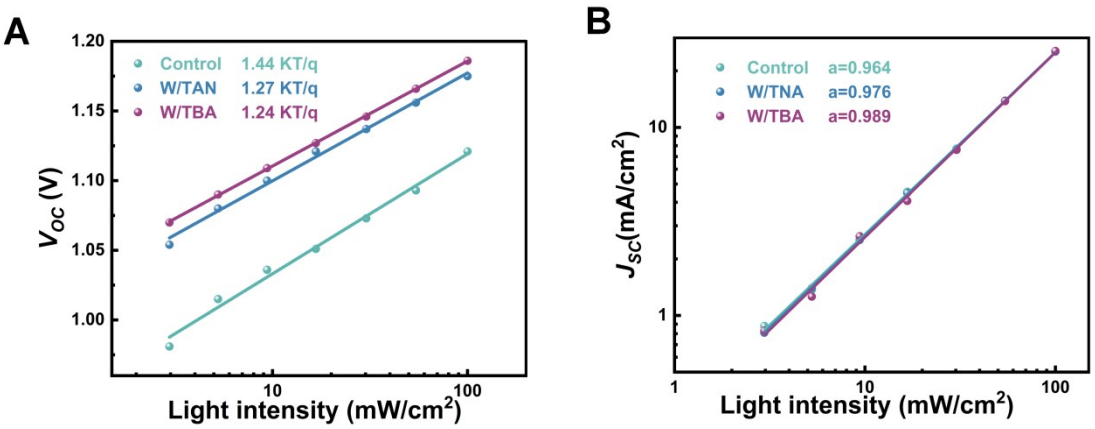

Figure S22. The light intensity dependence of the devices. (A) V_{oc} versus light intensity of the devices. (B) J_{sc} versus light intensity of the devices.

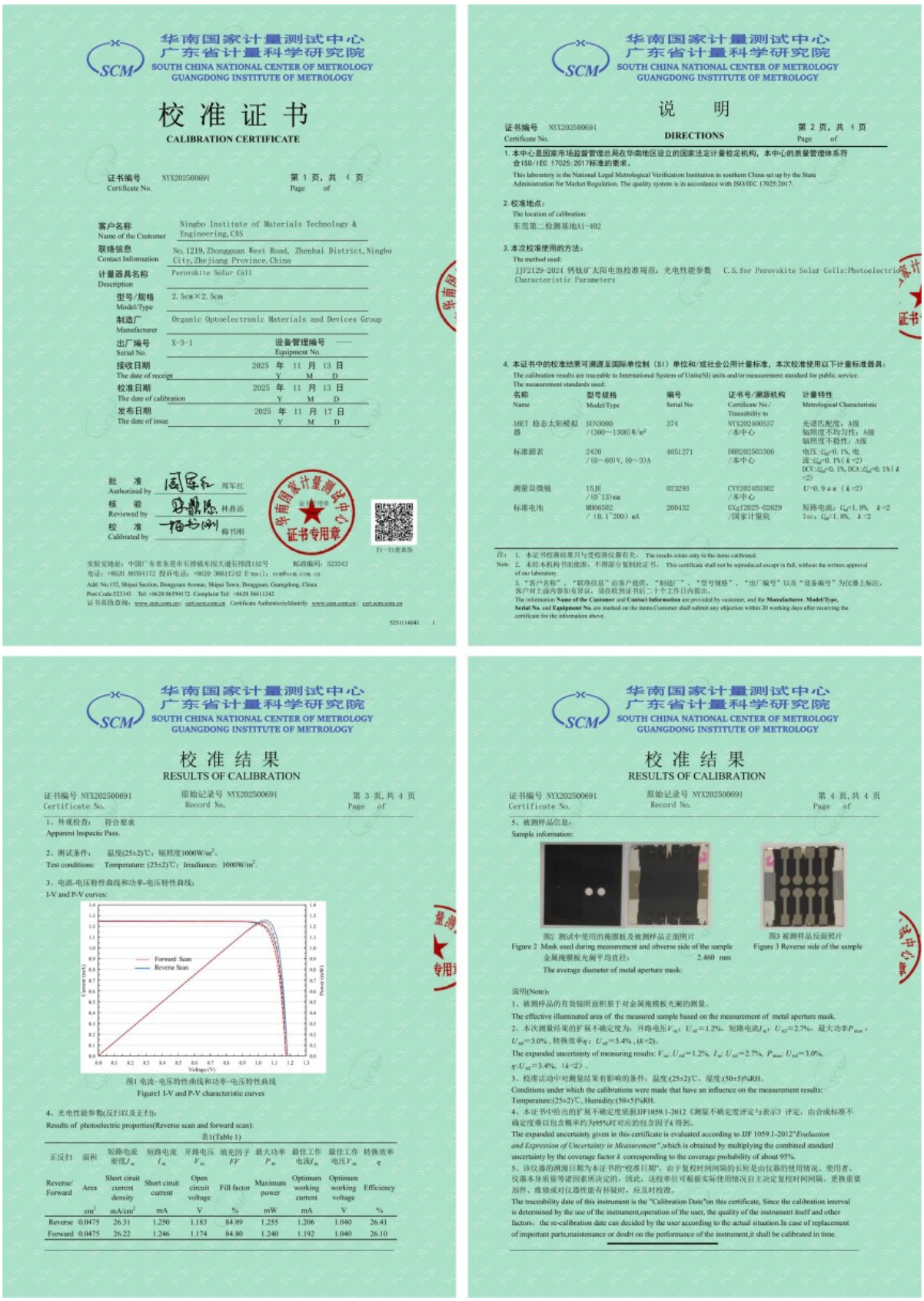

Figure S23. Independent efficiency certification of perovskite solar cells by an accredited institute of South China National Center of Metrology, giving a PCE of 26.41% of the champion device.

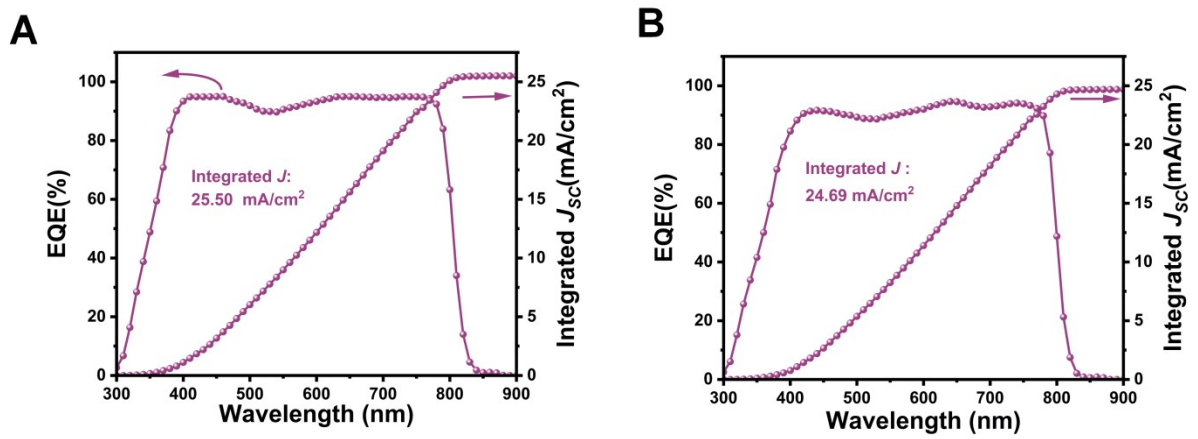

Figure S24. EQE spectra and corresponding integrated current density of rigid PSCs. (A) Rigid PSCs. (B) Flexible PSCs.

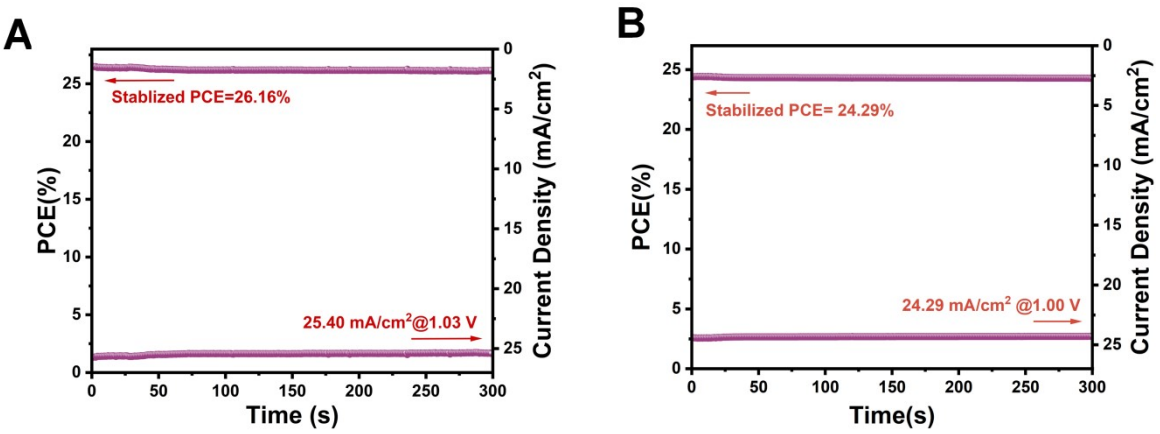

Figure S25. **The stable power output and steady-state current density of the best-performance rigid device with TBA**. (A) Rigid PSCs. (B) Flexible PSCs.

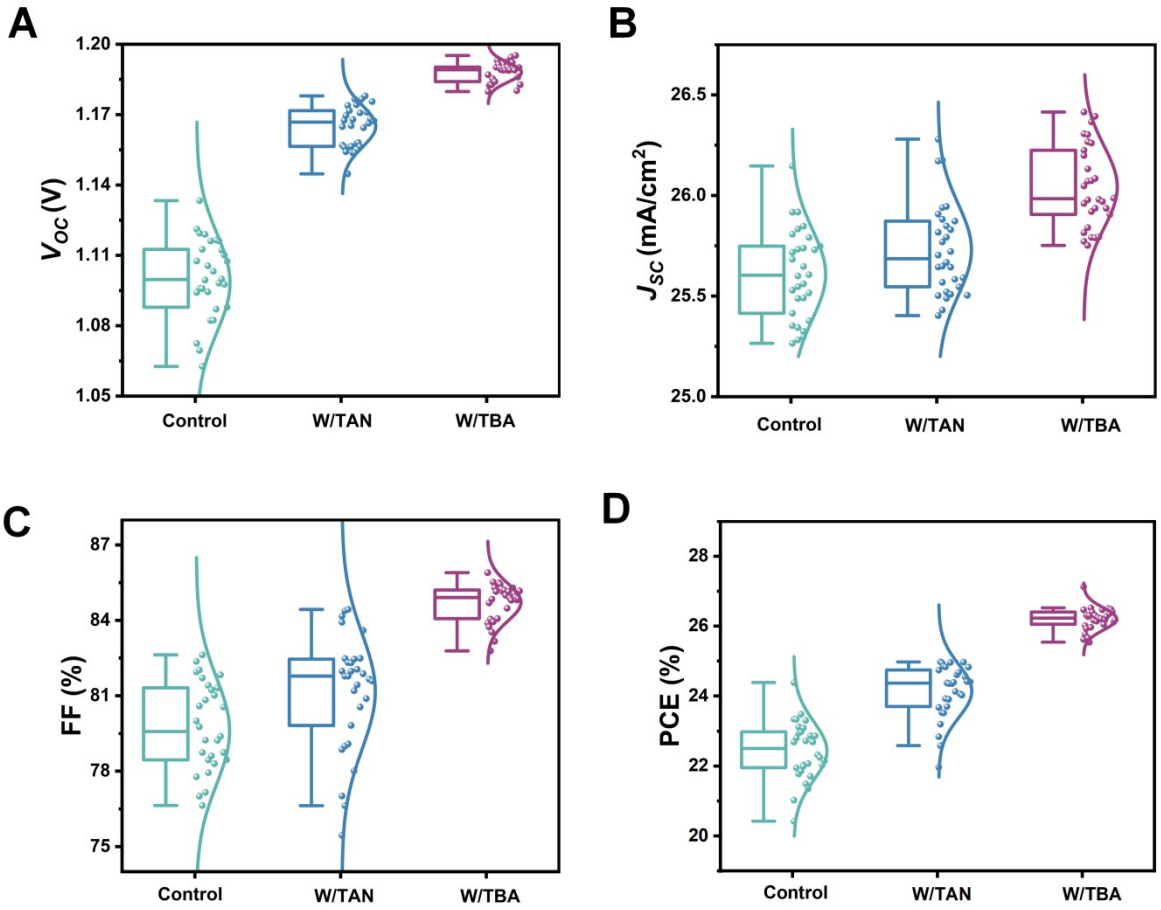

Figure S26. Statistical distribution of photovoltaic parameters from 30 individual rigid devices. (A) V_{oc} normal distribution. (B) J_{sc} normal distribution. (C) FF normal distribution. (D) PCE normal distribution.

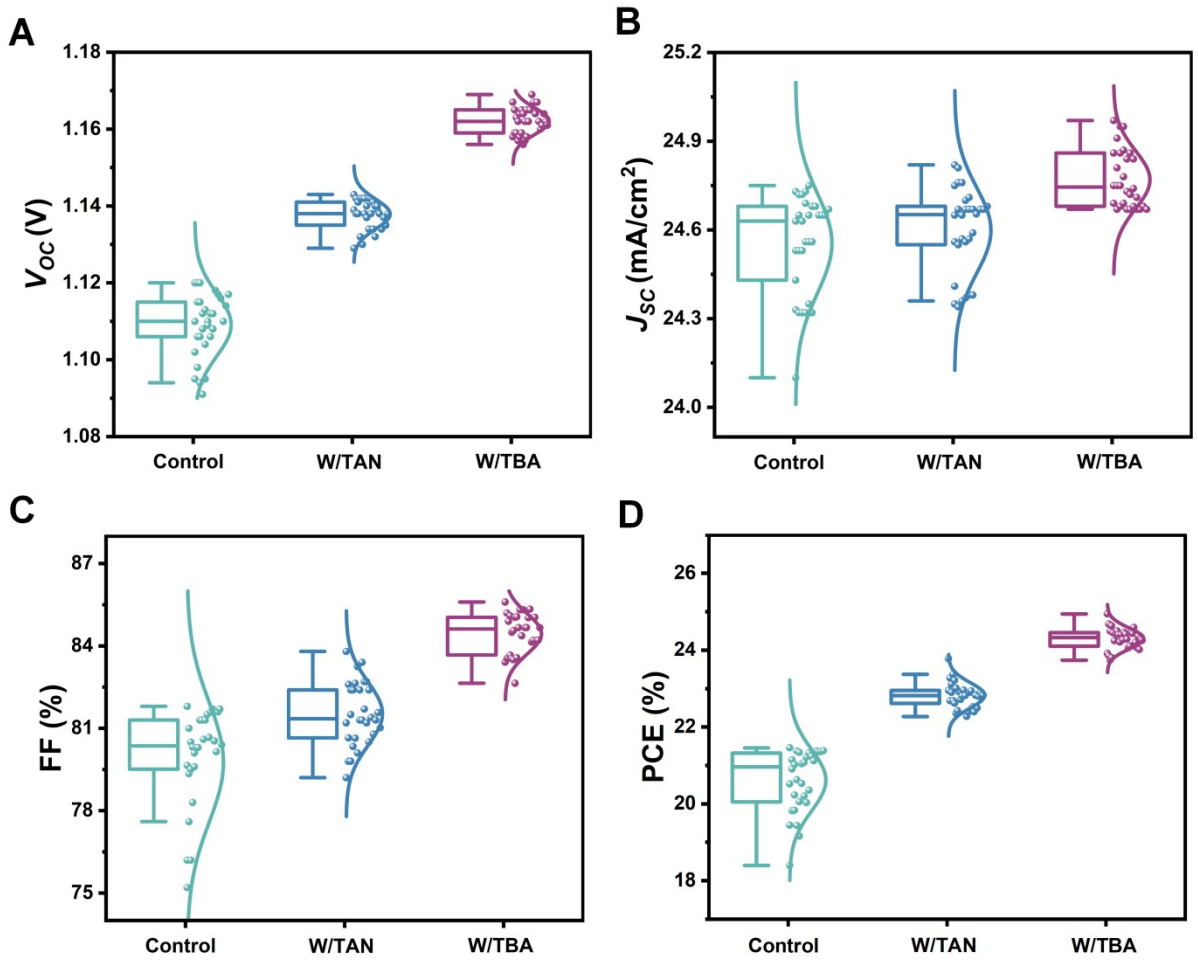

Figure S27. Statistical distribution of photovoltaic parameters from 30 individual flexible devices. (A) V_{oc} normal distribution. (B) J_{sc} normal distribution. (C) FF normal distribution. (D) PCE normal distribution.

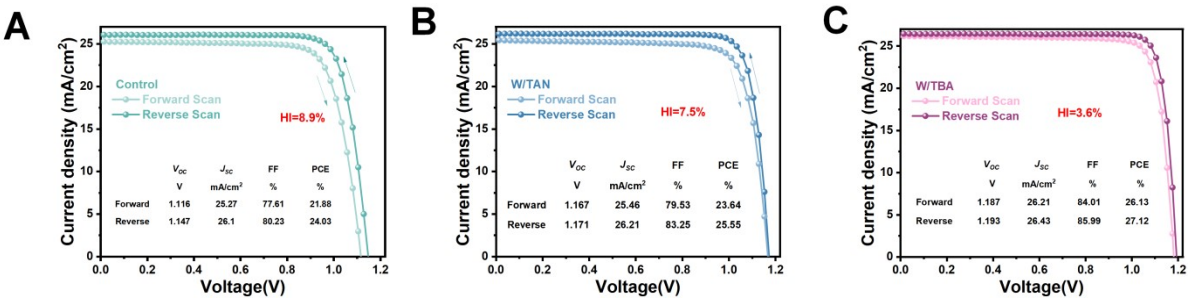

	V_{OC} (V)	J_{SC} (mA/cm²)	FF (%)	PCE (%)
Forward	1.116	25.27	77.61	21.88
Reverse	1.147	26.1	80.23	24.03

	V_{OC} (V)	J_{SC} (mA/cm²)	FF (%)	PCE (%)
Forward	1.167	25.46	79.53	23.64
Reverse	1.171	26.21	83.25	25.55

	V_{OC} (V)	J_{SC} (mA/cm²)	FF (%)	PCE (%)
Forward	1.187	26.21	84.01	26.13
Reverse	1.193	26.43	85.99	27.12

Figure S28. *J-V* curves with forward and reverse scan for devices. (A) Control, (B) W/TAN, (C) W/TBA-treated PSCs.

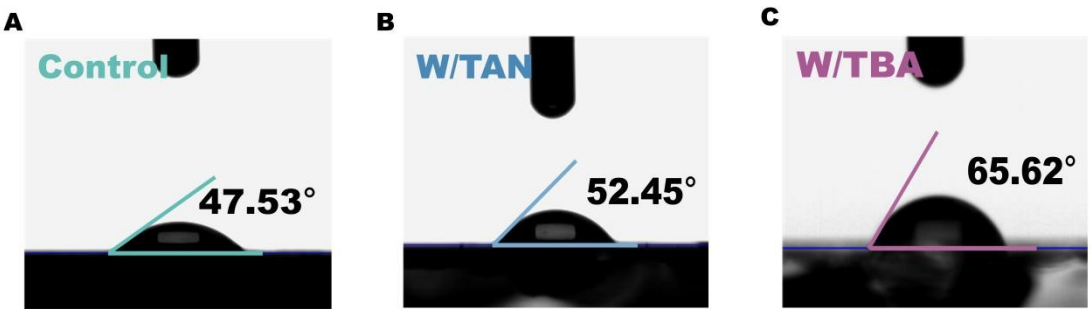

Figure S29. Water contact angles perovskite films.

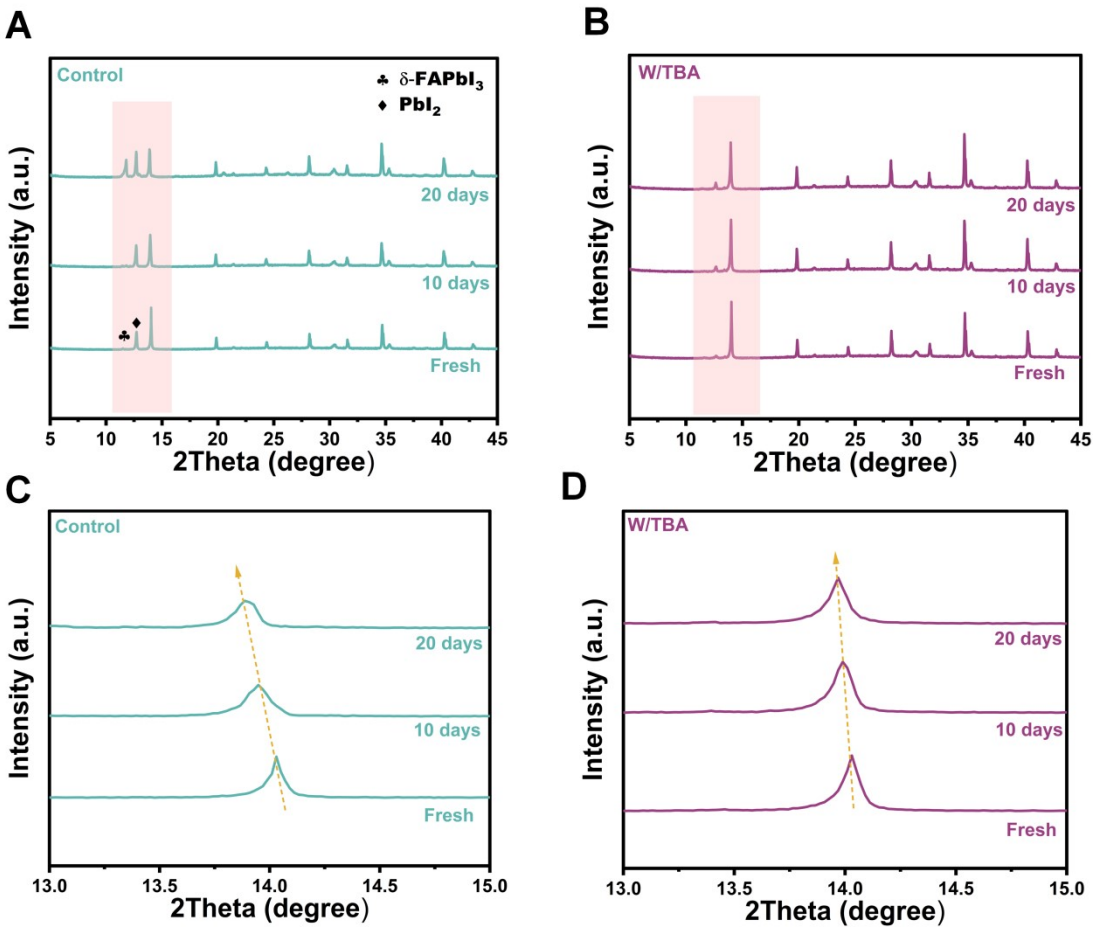

Figure S30. XRD patterns of the perovskite films during the accelerated aging process (air, 1-sun, 50% RH). (A) Control sample. (B) W/TBA sample. The evolution of the α-phase peak inthe XRD spectra of perovskite film.(C) Control sample. (D) W/TBA sample

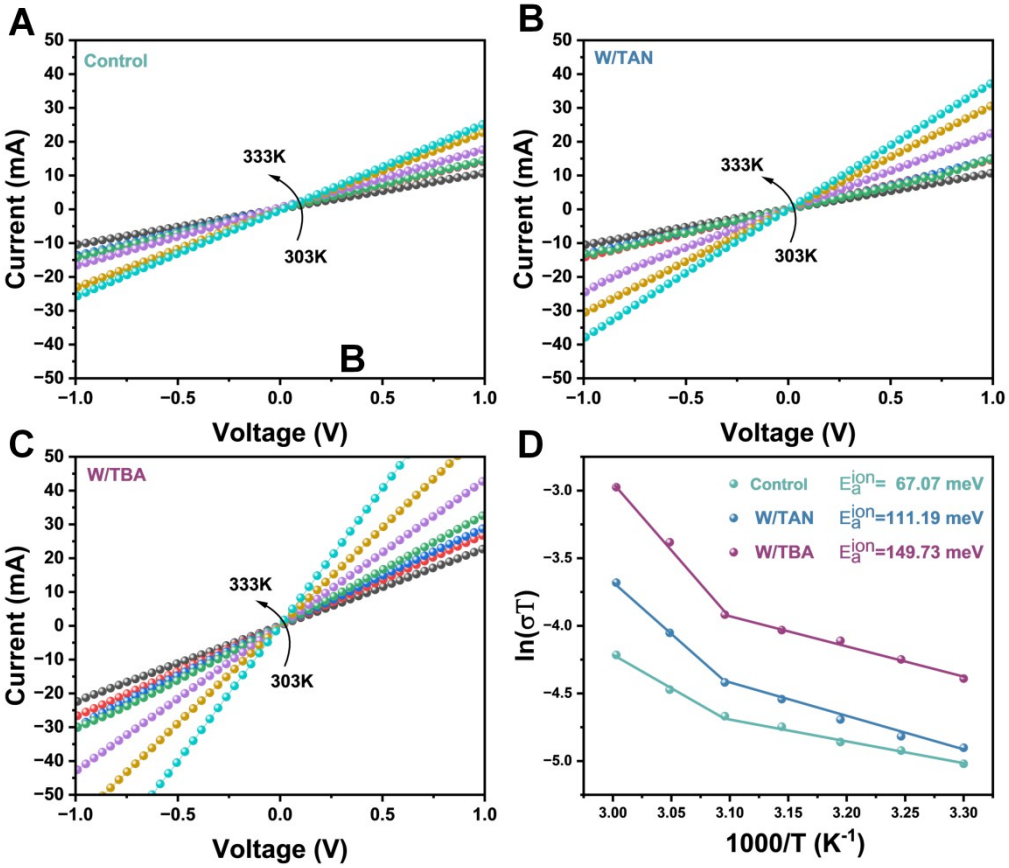

Figure S31. Temperature-dependent conductivity of the perovskite films (A) Control, (B) W/TAN, and (C) W/TBA. Devices of ITO/perovskite/Ag were used. (D) Ion migration activation energy of the perovskite films.

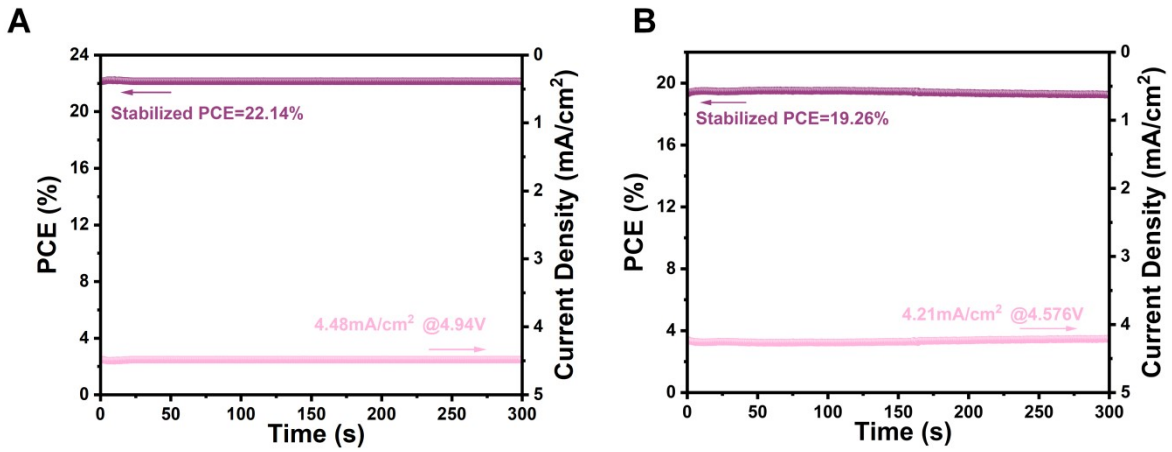

Figure S32. The stable power output and steady-state current density of the best-performance PSMs. (A) Rigid PSMs. (B) Flexible PSMs.

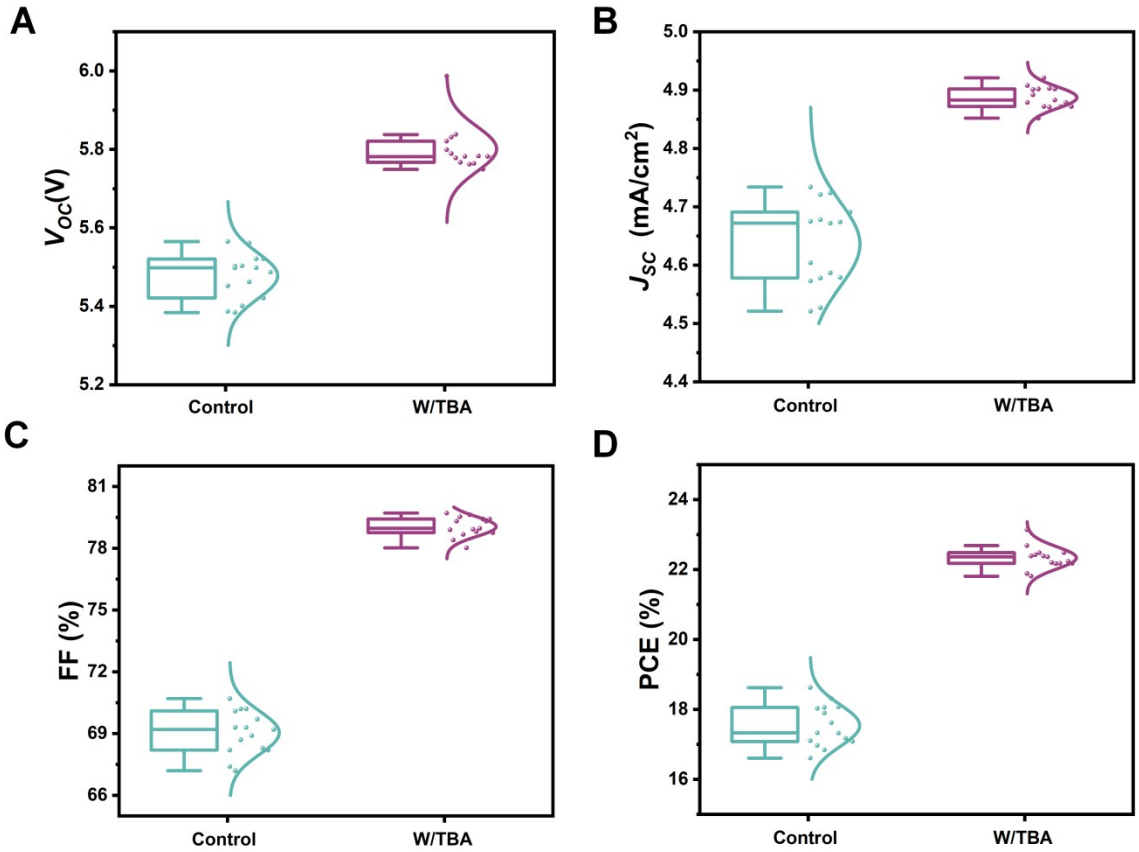

Figure S33. Statistical comparison of control and target-based perovskite mini-module with aperture area 10.24 cm^2 (the statistical results are obtained from 15 rigid mini-modules for each condition) (A) V_{oc} normal distribution. (B) J_{sc} normal distribution. (C) FF normal distribution. (D) PCE normal distribution.

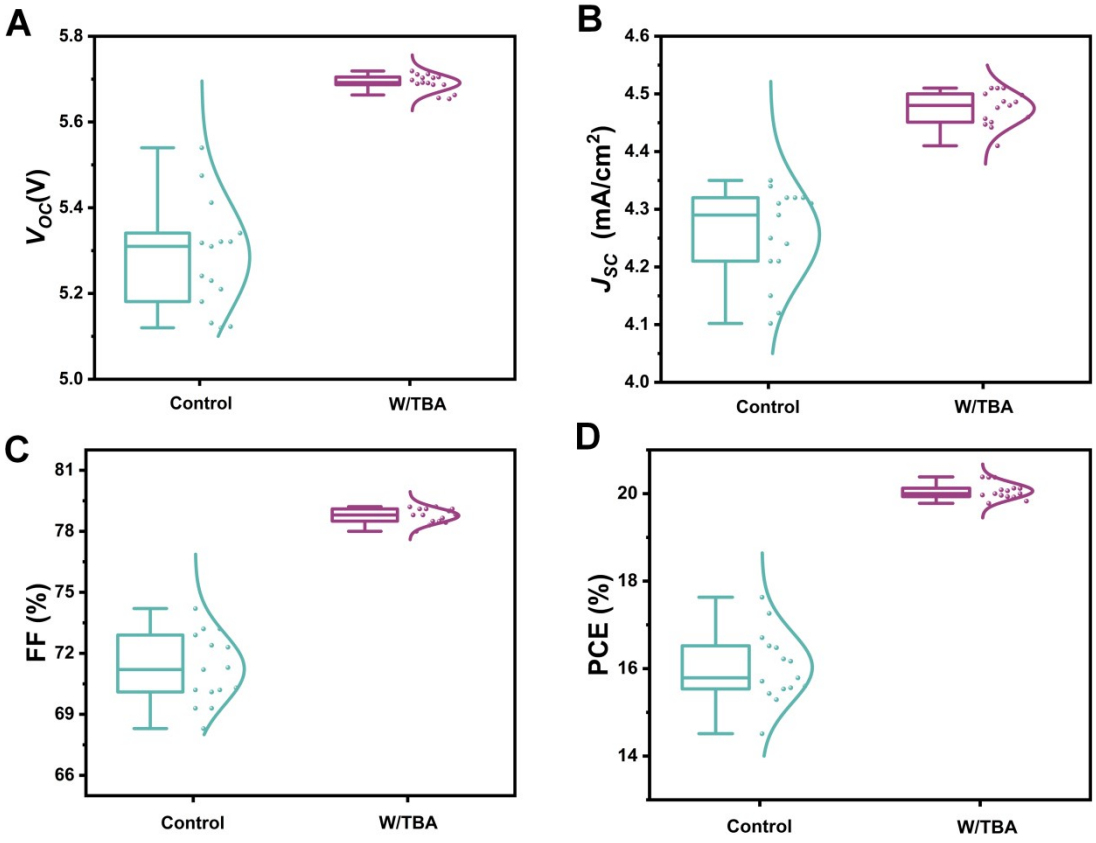

Figure S34. Statistical comparison of control and target-based perovskite mini-module with aperture area 10.24 cm^2 (the statistical results are obtained from 15 flexible mini-modules for each condition) (A) V_{oc} normal distribution. (B) J_{sc} normal distribution. (C) FF normal distribution. (D) PCE normal distribution.

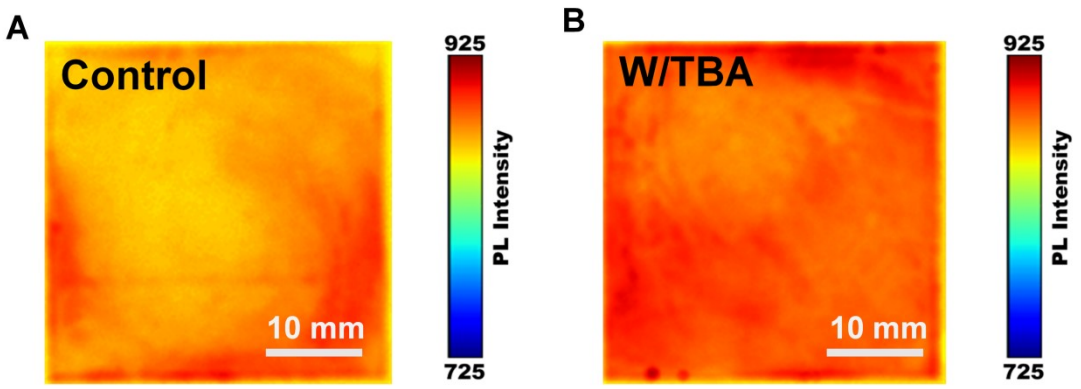

Figure S35. PL mapping images of perovskite films spin-coated on 50×50 mm^2 substrate. (A) Control, (B) W/TBA.

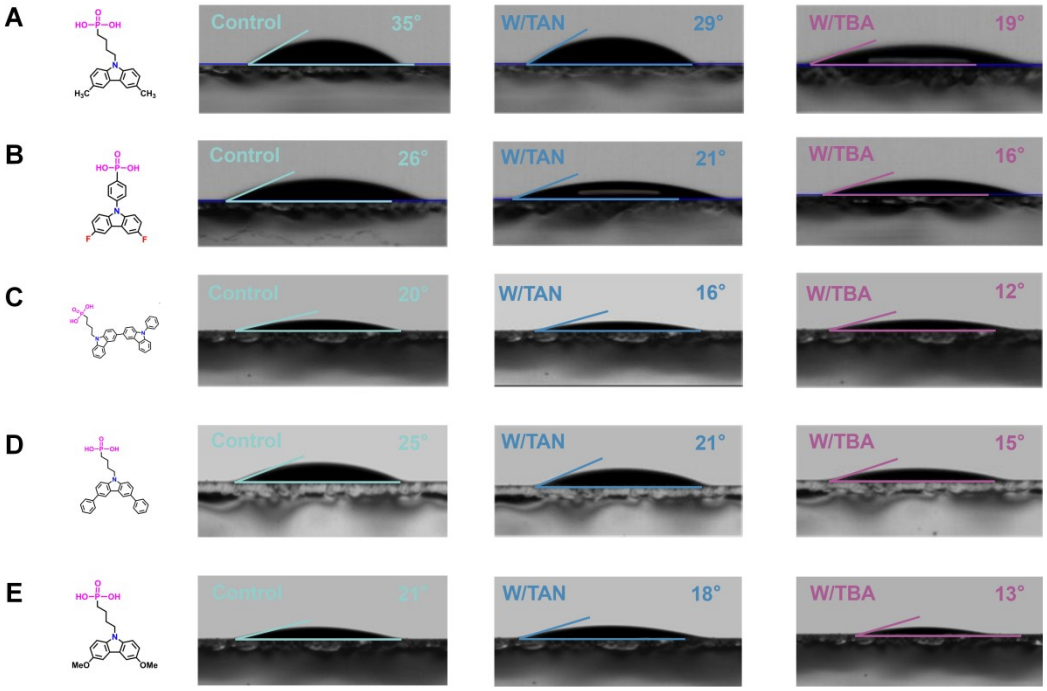

Figure S36. Contact angles of the perovskite precursor on the glass/ITO/SAM substrates. (A) Me-4PACz, (B) F-PhpPACz, (C) 4PABCz, (D) Ph-4PACz, (E) MeO-4PACz.

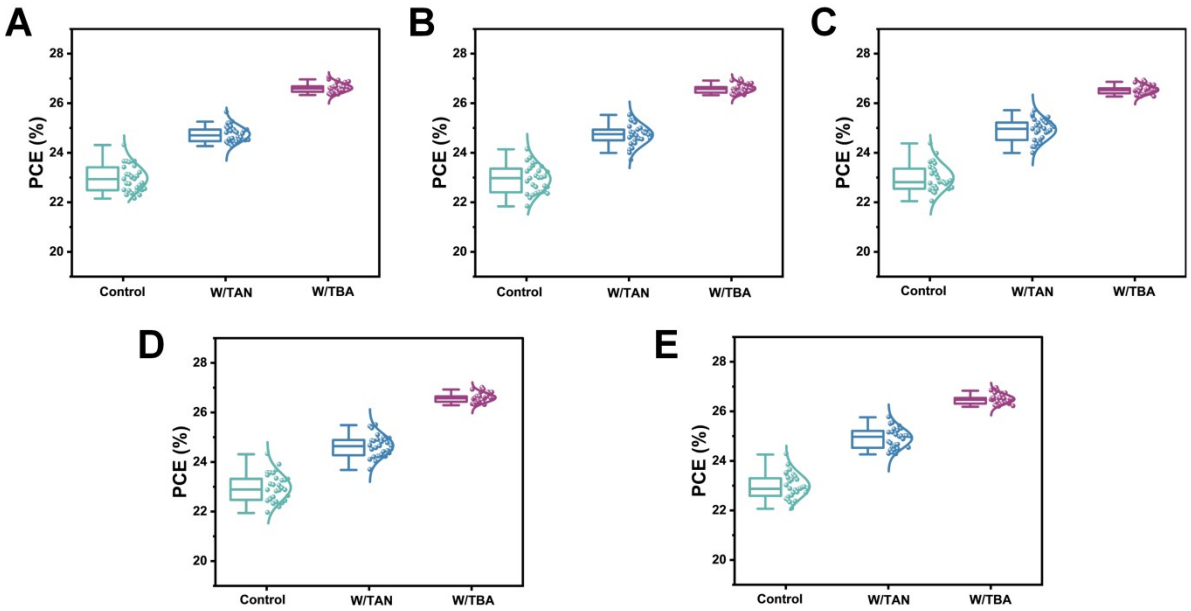

Figure S37. Statistical Distribution of Photovoltaic Parameters of 30 Independent Rigid Devices on Different SAMs. (A) Me-4PACz, (B) F-PhpPACz, (C) 4PABCz, (D) Ph-4PACz, (E) MeO-4PACz.

Smaple	A_1	τ_1	A_2	τ_2	τ_{ave}(ns)
Control	0.18 ±0.01	32.31 ±2.03	0.35 ±0.01	601.89 ±3.42	585.87 ±2.34
W/TAN	0.11 ±0.01	45.31 ±4.25	0.40 ±0.01	713.07 ±4.41	701.80 ±4.23
W/TBA	0.05 ±0.01	133.89 ±37.99	0.38 ±0.01	925.95 ±19.62	859.52 ±34.23

Table S1. Fitting carrier lifetimes of perovskite films determined by TRPL.

Table S2. R_1 and R_2 values from electrochemical impedance spectroscopy (EIS) data of the control, TAN-treated, and TBA-treated devices.

Sample	$R_1(\Omega)$	$R_2(\Omega)$
Control	43.52	1169
W/TAN	41.32	3290
W/TBA	23.54	5000

Table S3. Results derived from electronic-only SCLC.

Sample	V_{TFL} (V)	N_t (cm^{-3})
Control	0.75	1.11×10^{16}
W/TAN	0.69	1.02×10^{16}
W/TBA	0.53	7.88×10^{15}

Table S4. The dependence of V_{oc} and J_{sc} of the PSCs on light intensity.

Sample	*nkT/q*	α
Control	1.44kT/q	0.964
W/TAN	1.27kT/q	0.976
W/TBA	1.24kT/q	0.989

Table S5. Statistics of photovoltaic parameters for 30 individual perovskite solar cells (PSCs)

Sample	V_{oc} (V)	J_{sc} (mA/cm^2)	FF (%)	PCE (%)
Control	1.099±0.034	25.36±0.028	79.60±3.04	22.17±1.29
W/TAN	1.170±0.080	25.52±0.025	81.80±2.66	24.07±1.01
W/TBA	1.183±0.057	25.67±0.022	84.91±1.04	26.43±0.69

Table S6. Statistics of photovoltaic parameters for 30 individual flexible PSCs.

Sample	V_{oc} (V)	J_{sc} (mA/cm^2)	FF (%)	PCE (%)
Control	1.083±0.034	24.36±0.028	77.54±2.78	21.47±1.19
W/TAN	1.132±0.080	24.47±0.025	80.61±2.66	22.71±1.07
W/TBA	1.163±0.057	24.67±0.022	84.91±1.04	24.03±0.92

Table S7. Detailed photovoltaic parameters for the best performing rigid PSCs.

	Scanning	V_{oc} (V)	J_{sc} (mA/cm^2)	FF (%)	PCE (%)	HI (%)
Control	Reverse	1.147	26.1	80.23	24.03	8.9
	Forward	1.116	25.27	77.60	21.88	
W/TAN	Reverse	1.174	26.21	83.25	25.55	7.5
	Forward	1.167	25.46	79.53	23.64	
W/TBA	Reverse	1.192	26.43	85.99	27.12	3.6
	Forward	1.187	26.21	84.01	26.13	

Table S8. Summary of photovoltaic parameters of reported high-performance inverted PSMs up to now (active areas are 10-100 cm^2)

Device Architecture	V_{oc} (V)	J_{sc} (mA/cm^2)	FF (%)	PCE (%)	Area (cm^2)	Ref.
Glass/ITO/SAM/Perovskite/C_{60}/BCP/Ag	**5.987**	**4.86**	**79.4**	**23.10**	**10.24**	**This work**
Glass/ITO/SAM/Perovskite/C_{60}/BCP/Ag	5.686	4.85	79.48	21.92	10.24	[1]
Glass/FTO/NiOx/Al_2O_3/SAM/Perovskite/C_{60}/BCP/Cr/Bi/Cu	5.82	4.78	81.46	22.66	11.09	[2]
Glass/FTO/NiO/SAM/Perovskite/PCBM/BCP/Cu	5.799	4.83	78.99	22.08	11.1	[3]
Glass/ITO/Me-4PACz/Perovskite/LiF /C_{60}/SnO*x*/Cu	8.35	3.06	66.87	17.13	12.7	[4]
Glass/ITO/SAM/Perovskite/LiF /C_{60}/SnO_2/Cu	-	-	66.80	17.10	12.70	[5]
glass/FTO/Ph-4PACz/Perovskite/C_{60}/BCP/Ag	7.08	4.09	74.96	21.72	16	[6]
Glass/ITO/SA-BPP/Perovskite /PCBM/C_{60}/BCP/Ag	2.87	7.59	77.51	17.08	22.4	[7]
Glass/ITO/NiOx/Me-4PACz/Perovskite /C_{60}/BCP/Cu	12.83	2.15	71.84	19.83	40.1	[2]
Glass/ITO/PTAA/Perovskite/C_{60}/BCP/Cu	23.40	1.073	80.1	20.11	78	[8]

Table S9. Summary of photovoltaic parameters of reported high-performance inverted f-PSMs up to now (active areas are 5-100 cm^2)

Device Architecture	V_{oc} (V)	J_{sc} (mA/cm^2)	FF (%)	PCE (%)	Area (cm^2)	Ref.
PEN/ITO/SAM/Perovskite/C_{60}/BCP/Ag	**5.719**	**4.50**	**79.2**	**20.38**	**10.24**	**This work**
PET/ITO/PTAA/Perovskite/C_{60}/BCP/Cu	-	-	-	20.10	9.00	[9]
PET/ITO/PTAA/Perovskite/C_{60}/BCP/Cu	-	-	-	18.7	21.00	[9]
PET/ITO/PTAA/Perovskite/C_{60}/BCP/Cu	-	-	-	17.8	32.40	[9]
PEN/ITO/Bio-IL/Perovskite/PCBM/BCP/Ag	5.39	4.52	69.26	16.87	14.63	[10]
PEN/ITO/SAM/Perovskite/2D-passivation/C_{60}/BCP/Ag	8.123	3.17	75.57	19.51	20.48	[11]
MgF2/Willow PEN/ITO/PTAA/Perovskite/C_{60}/BCP/Cu	13.142	1.64	73.5	15.86	42.90	[12]
PEN/ITO/SAM/Perovskite/C_{60}/BCP/Ag	5.584	4.40	69.7	17.13	10.24	[13]

Table S10. Statistics of photovoltaic parameters for 15 individual perovskite solar modules (PSMs)

Sample	V_{oc} (V)	J_{sc} (mA/cm^2)	FF (%)	PCE (%)
Control	5.56±0.107	4.64±0.180	71.09±4.61	17.59±2.95
W/TBA	5.76±0.037	4.89±0.031	78.91±0.75	22.66±0.44

Table S11. Statistics of photovoltaic parameters for 15 individual flexible perovskite solar modules (f-PSMs)

Sample	V_{oc} (V)	J_{sc} (mA/cm^2)	FF (%)	PCE (%)
Control	5.20±0.275	4.14±0.2	70.09±4.11	16.59±1.04
W/TBA	5.61±0.109	4.41±0.09	77.91±1.299	19.75±0.63

Reference

1 S. Du, X. Tong, W. Zhang, X. Yan, Y. Zhou, J. Ge, Y. Luan, H. Guan, M. Yang, H. Liang, L. Xie and Z. Ge, *Adv. Energy Mater.*, 2025, e03781.

2 W. Liu, R. Chen, Z. Tan, J. Wang, S. Liu, C. Shi, X. Liu, Y. Cai, F. Ren, Z. Zhou, Q. Zhou, W. Li, T. Miao, H. Zhu, T. Imran, Z. Liu and W. Chen, *Adv. Energy Mater.*, 2025, **15**, 2404374.

3 Z. Tan, W. Liu, R. Chen, S. Liu, Q. Zhou, J. Wang, F. Ren, Y. Cai, C. Shi, X. Liu, Z. Zhou, H. Zhu, T. Miao, W. Li, M. Wang, Z. Liu and W. Chen, *Adv. Funct. Mater.*, 2025, **35**, 2419133.

4 J. Li, J. Dagar, O. Shargaieva, O. Maus, M. Remec, Q. Emery, M. Khenkin, C. Ulbrich, F. Akhundova, J. A. Márquez, T. Unold, M. Fenske, C. Schultz, B. Stegemann, A. Al-Ashouri, S. Albrecht, A. T. Esteves, L. Korte, H. Köbler, A. Abate, D. M. Többens, I. Zizak, E. J. W. List-Kratochvil, R. Schlatmann and E. Unger, *Adv. Energy Mater.*, 2023, **13**, 2203898.

5 H. Hu, D. B. Ritzer, A. Diercks, Y. Li, R. Singh, P. Fassl, Q. Jin, F. Schackmar, U. W. Paetzold and B. A. Nejand, *Joule*, 2023, **7**, 1574–1592.

6 Z. Zhu, B. Ke, K. Sun, C. Jin, Z. Song, R. Jiang, J. Li, S. Kong, C. Liu, S. Bai, S. He, Z. Ge, F. Huang, Y.-B. Cheng and T. Bu, *Energy Environ. Sci.*, 2025, **18**, 4120–4129.

7 T. Wu, X. Xu, L. K. Ono, T. Guo, S. Mariotti, C. Ding, S. Yuan, C. Zhang, J. Zhang, K. Mitrofanov, Q. Zhang, S. Raj, X. Liu, H. Segawa, P. Ji, T. Li, R. Kabe, L. Han, A. Narita and Y. Qi, *Adv. Mater.*, 2023, **35**, 2300169.

8 M. A. Uddin, P. J. S. Rana, Z. Ni, G. Yang, M. Li, M. Wang, H. Gu, H. Zhang, B. D. Dou and J. Huang, *Nat. Commun.*, 2024, **15**, 1355.

9 W. Xu, B. Chen, Z. Zhang, Y. Liu, Y. Xian, X. Wang, Z. Shi, H. Gu, C. Fei, N. Li, M. A. Uddin, H. Zhang, L. Dou, Y. Yan and J. Huang, *Nat. Photonics*, 2024, **18**, 379–387.

10 B. Fan, J. Xiong, Y. Zhang, C. Gong, F. Li, X. Meng, X. Hu, Z. Yuan, F. Wang and Y. Chen, *Adv. Mater.*, 2022, **34**, 2201840.

11 D. Gao, B. Li, Z. Li, X. Wu, S. Zhang, D. Zhao, X. Jiang, C. Zhang, Y. Wang, Z. Li, N. Li, S. Xiao, W. C. H. Choy, A. K. -Y. Jen, S. Yang and Z. Zhu, *Adv. Mater.*, 2023, **35**, 2206387.

12 X. Dai, Y. Deng, C. H. Van Brackle, S. Chen, P. N. Rudd, X. Xiao, Y. Lin, B. Chen and J. Huang, *Adv. Energy Mater.*, 2020, **10**, 1903108.

13 W. Zhang, J. Liu, W. Song, J. Shan, H. Guan, J. Zhou, Y. Meng, X. Tong, J. Zhu, M. Yang and Z. Ge, *Sci. Adv.*, 2025, **11**, eadr2290.